Supporting Information

Spinel $ZnMn_2O_4$/Ni-based Metal Organic Framework Hybrid Composite for High-Performance Asymmetric Supercapacitors

Abinash Kumararaj[1], Kamala Bharathi Karuppanan[2], Geetha Arunachalam[1]*

[1,1*] Department of Physics and Nanotechnology, Faculty of Engineering and Technology, SRM Institute of Science and Technology, Kattankulathur, Chengalpattu 603 203.

[2]Thin Film Energy Storage Laboratory, Department of Physics and Nanotechnology, SRM Institute of Science and Technology, Kattankulathur, Chengalpattu 603 203, Tamil Nadu, India

*Corresponding author e-mail: geethaa@srmist.edu.in

Materials	Synthesis method	Electrolyte	Specific Capacitance	Potential Window/ Retention	Ref
$ZnMn_2O_4$	sol–gel auto-combustion approach	1 M KOH	417.52 Fg^{-1} at 1 Ag^{-1}	0.4 V	1
$ZnMn_2O_4$ nanosheets	cathodic electrodeposition	0.5 M Na_2SO_4	457 Fg^{-1} at 1 Ag^{-1}	1 V	2
$ZnMn_2O_4$	Solvothermal	2 M KOH	187 Fg^{-1} at 1 Ag^{-1}	1.1 V	3
$ZnMn_2O_4/Mn_2O_3$	Hydrothermal	2 M KOH	380 Fg_{-1} at 0.5 Ag^{-1}	0.5 V	4
Mo-doped $ZnMn_2O_4$	Hydrothermal	1 M Na_2SO_4	545 Fg^{-1} at 1 $mAcm^{-2}$	0.6 V	5
Ni-MOF	Sono-chemical Approach	1M KOH	402 Fg^{-1} at 1 Ag^{-1}	0.35 V	6
Ni-MOF	One-step synthesis	3M KOH	318 Fg^{-1} at 1 Ag^{-1}	0.5 V	7
NiCo-BDC MOF	Hydrothermal	1M KOH	485 Fg^{-1} at 0.67 Ag^{-1}	0.6 V	8
Ni-MOF derived	Hydrothermal	6M KOH	435.25 Fg^{-1} at 1	0.4 V	9

NiO/rGO	followed by calcination		Ag^{-1}		
$ZnMn_2O_4$/Ni-MOF	**Hydrothermal**	**2 M KOH**	**623 Fg^{-1} at 1 Ag^{-1}**	**0.58 V**	**This Work**

Table 1. Literature comparison between the various other $ZnMn_2O_4$ and Ni-MOF-based materials with this work.

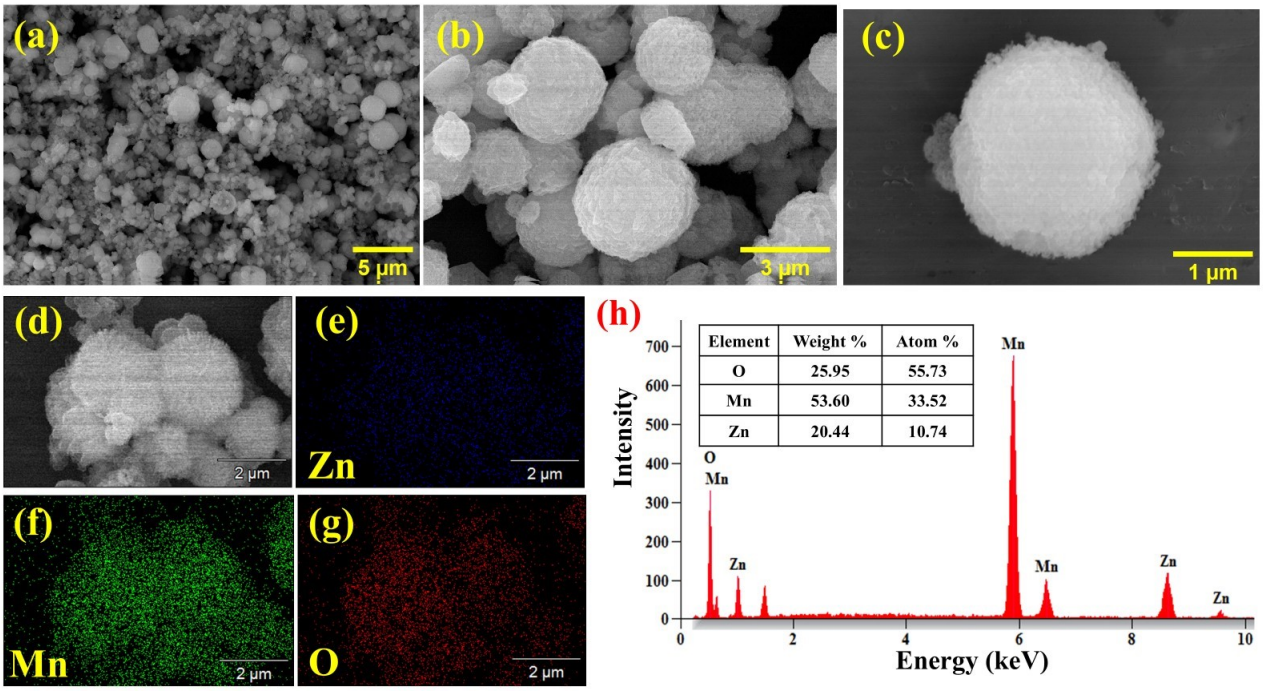

Figure S1. (a-c) HR-SEM images of $ZnMn_2O_4$ at different magnifications, (d-g) Elemental mapping images, (h) EDX spectrum, and elemental composition of $ZnMn_2O_4$.

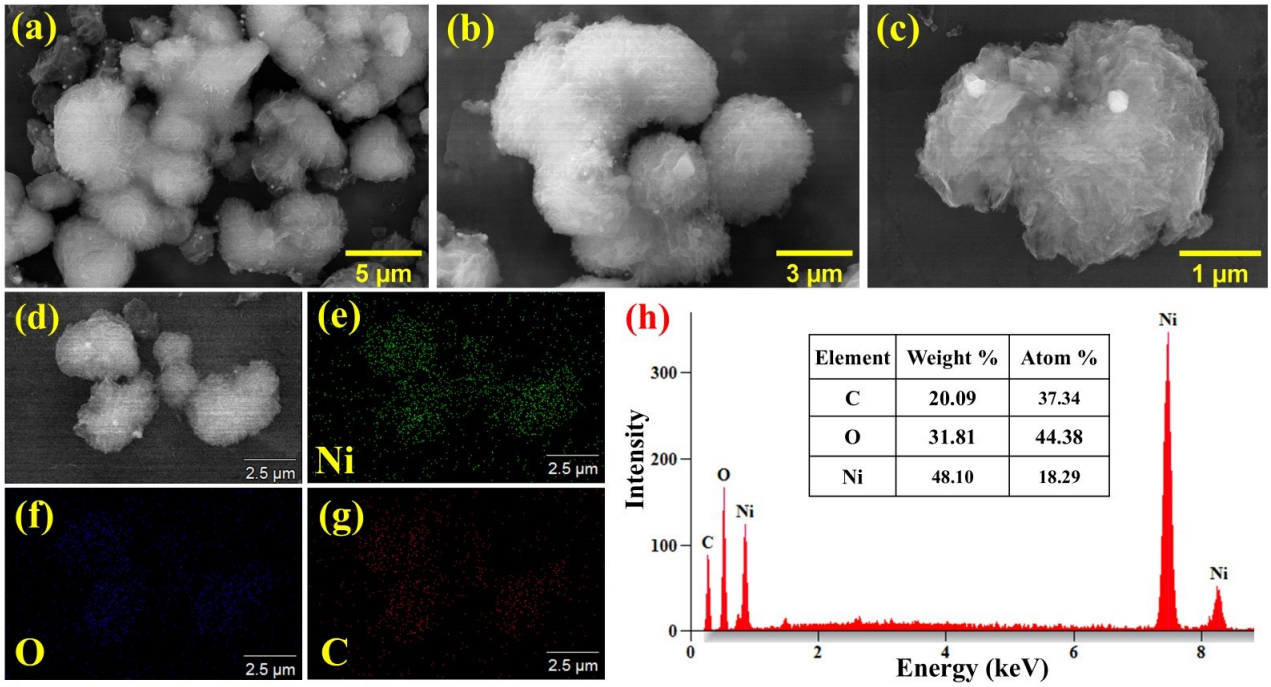

Figure S2. (a-c) HR-SEM images of Ni-MOF at different magnifications, (d-g) Elemental mapping images, (h) EDX spectrum, and elemental composition of Ni-MOF.

Electrochemical testing:

Researchers used the equation $i_p = av^b$, which was changed to $log(i_p) = log(a) + blog(v)$, to find the current contribution by finding the b-value (slope) from the plot between log(i_p) and log(ν). The letters 'i_p' stand for peak anodic/cathodic current, and 'ν' stands for scan rate. The b-value can be anywhere from 0.5 to 1. Values close to 0.5 are mostly due to the diffusion-controlled faradaic process, while values close to 1 are mostly due to the capacitive-controlled current.

Dunn's method is used to calculate current contribution percentages for different scan rates. The equation employed is:

$$i(v) = k_1 v + k_2 v^{\frac{1}{2}} \quad \textbf{S1}$$

$$\frac{i(v)}{v^{\frac{1}{2}}} = k_1 v^{\frac{1}{2}} + k_2 \quad \textbf{S2}$$

A graph has been plotted between $\frac{i(\nu)}{\nu^{\frac{1}{2}}}$ and $\nu^{\frac{1}{2}}$, with the slope of the linear fit yielding the k_1 value, while the y-intercept provides the k_2 value. From which the present contribution is computed.

Electrochemical testing was carried out with a 2M potassium hydroxide (KOH) electrolyte. The specific capacitance (C_S) of GCD was calculated using the following formula:

$$C_s = \frac{I\Delta t_d}{m(\Delta V)} \quad \textbf{S3}$$

In this context, 'I' signifies the current during the discharge process, 'Δt_d' represents the discharge duration, 'm' denotes the mass of the active material on the electrode, and 'ΔV' indicates the potential window of the material.

Coulombic efficiency:

$$\eta = \frac{\Delta t_d}{\Delta t_c} \quad \textbf{S4}$$

Δt_d (s) represents the discharge time, and Δt_c represents the charging time.

AASC and ASC Electrochemical preparation:

For the two-electrode investigations, activated carbon (AC) was employed as the active material on one side to evaluate supercapacitance performance, while the electrode preparation method was standardised to minimise mistakes and ensure reproducibility. In the manufacture of the asymmetric device, nickel foam was covered with $ZnMn_2O_4$/Ni-MOF to serve as the cathode, activated carbon (AC) was utilised as the anode, Whatman filter paper functioned as the separator, and PVA-KOH gel was employed as the electrolyte. To prepare the gel electrolyte, 1g of PVA is dissolved in 20 ml of deionised water while continuously stirring at 60˚C until a transparent solution is achieved. Subsequently, 2 M KOH dissolved in 15 ml of deionised water was added gradually until a homogeneous gel was achieved.

Fabrication and testing of an aqueous asymmetric supercapacitor (AASC):

AASC is basically a two-electrode setup using $ZnMn_2O_4$/Ni-MOF composite in NF as anode and activated carbon (AC) in NF as cathode in 2M KOH solution as the electrolyte. To receive optimal output from the AASC, a charge equilibrium must be maintained between the two electrodes ($q^+ = q^-$), which is contingent upon the mass loading ratio (m^+/m^-). The specific

capacitance of AC and $ZnMn_2O_4$/Ni-MOF composite was evaluated using a three-electrode setup to determine the ideal mass ratio of the positive and negative electrode materials. The mass ratio was calculated using the following equation:

$$\frac{m^+}{m^-} = \frac{C^- \Delta V^-}{C^- \Delta V^+} \quad \text{- S5}$$

Where C^- and C^+ are specific capacitance, ΔV^- and ΔV^+ is the potential window of the AC and $ZnMn_2O_4$/Ni-MOF composite, respectively.

Energy Density (Wh/Kg):

$$E_d = \frac{1}{2} C_S \Delta V^2 \quad \text{- S6}$$

Where 'E_d' represents the energy density, 'C_S' is specific capacitance, and 'ΔV' is the potential window.

Power Density (W/Kg):

$$P_d = \frac{E_d}{\Delta t_d} \quad \text{- S7}$$

Where 'P_d' represents the power density, 'E_d' is the energy density, and 'Δt_d' is the discharging time.

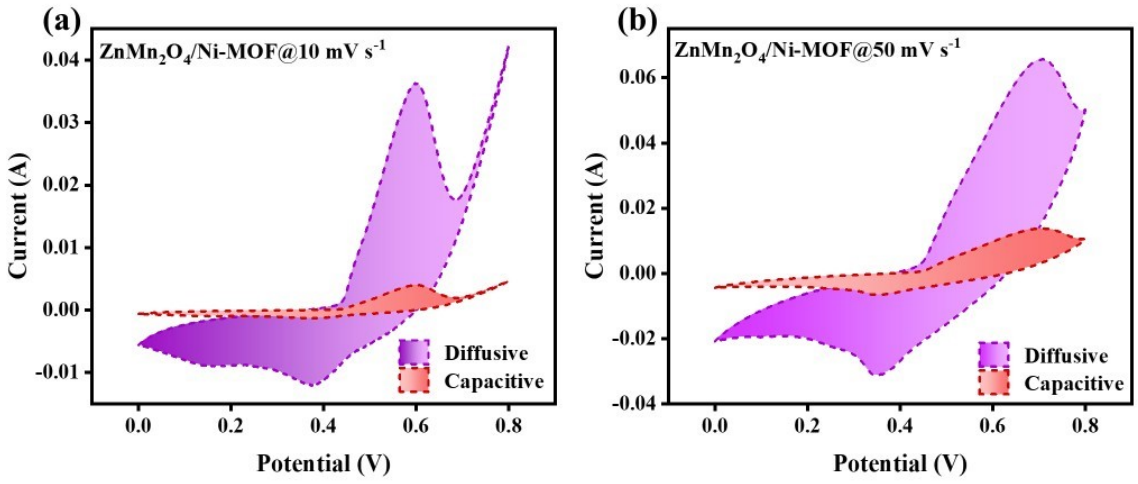

Figure S3. (a, b) CV curves of diffusion and current contribution for 10 and 50 mVs^{-1} scan rates of $ZnMn_2O_4$/Ni-MOF composite.

The electrochemical performance of $ZnMn_2O_4$ is evaluated using a three-electrode configuration. The CV analysis of the $ZnMn_2O_4$ is conducted at scan rates ranging from 10 to 50 mV s^{-1}, with a potential of 0.7 V (vs Ag/AgCl) in 2 M KOH, as shown in **Figure S4a**. Increasing scan rates reveal identifiable redox peaks, confirming the distinctive

pseudocapacitive behaviour due to rapid charge-transfer kinetics. The Randles-Sevcik equation calculates the connection between peak current (i_p) and the square root of scan rate ($v^{1/2}$) in both anodic and cathodic responses. As the scan rate increases from 10 to 50 mVs^{-1}, the anodic peak of the $ZnMn_2O_4$ shifts from 0.459 V to 0.56 V, indicating a potential shift of 0.101 V, as illustrated in **Figure S4b**. The noted increase in anodic peak potentials for the $ZnMn_2O_4$ signifies a distinctive pseudocapacitive behavior affected by electrochemical kinetics. The b-value of the $ZnMn_2O_4$ is found to be 0.514 (**Figure S4c**), which shows both battery and pseudocapacitive behaviour, indicating both diffusion and surface-controlled faradaic reactions. Dunn's method is employed to measure the current contributions from surface-controlled and diffusion-controlled processes utilizing **Equations S1 & 2** in the composite (**Figure S4d**). The bar graph demonstrates that as the scan rate rises from 10 to 50 mV s^{-1}, the diffusion-controlled current diminishes from 31 % to 17 % owing to increasing internal diffusion resistance, and the capacitive current increases from 69 % to 83 %, as shown in **Figure S4e.** The current contributions of $ZnMn_2O_4$ are well seen in the CV graphs as shown in **Figure S4f, g** for scan rates of 10 and 50 mV s^{-1}. The GCD analysis of the $ZnMn_2O_4$ is taken at different current densities of 1 to 6 A g^{-1}, as shown in **Figure S4h**, and it shows a higher specific capacitance of 232 A g^{-1} at 1 Ag^{-1}, using **Equation S3**. The specific capacitance of $ZnMn_2O_4$ at different current densities is shown in **Figure S4i**. Electrochemical impedance spectroscopy (EIS) is conducted within a frequency range of 100 kHz to 100 mHz to examine the electron-transfer kinetics, interfacial interactions, and capacitive characteristics of the electrode material, as depicted in the Nyquist plot in **Figure. S4j**. The solution resistance R_s of the $ZnMn_2O_4$ is found to be 1.062 Ω before cycling and 1.089 Ω after cycling, and the charge transfer resistance (R_{ct}) of the $ZnMn_2O_4$ is determined to be 8.42 Ω before cycling and 8.52 Ω after cycling. The capacitance retention (CR) and coulombic efficiency (CE) of the $ZnMn_2O_4$ electrode material were evaluated across 5000 charge-discharge cycles at a current density of 10 A g^{-1}. The electrode exhibited a CR of 80 % and a CE of 94 %, as calculated using **Equation S4**, as illustrated in the F**igure. S4k**.

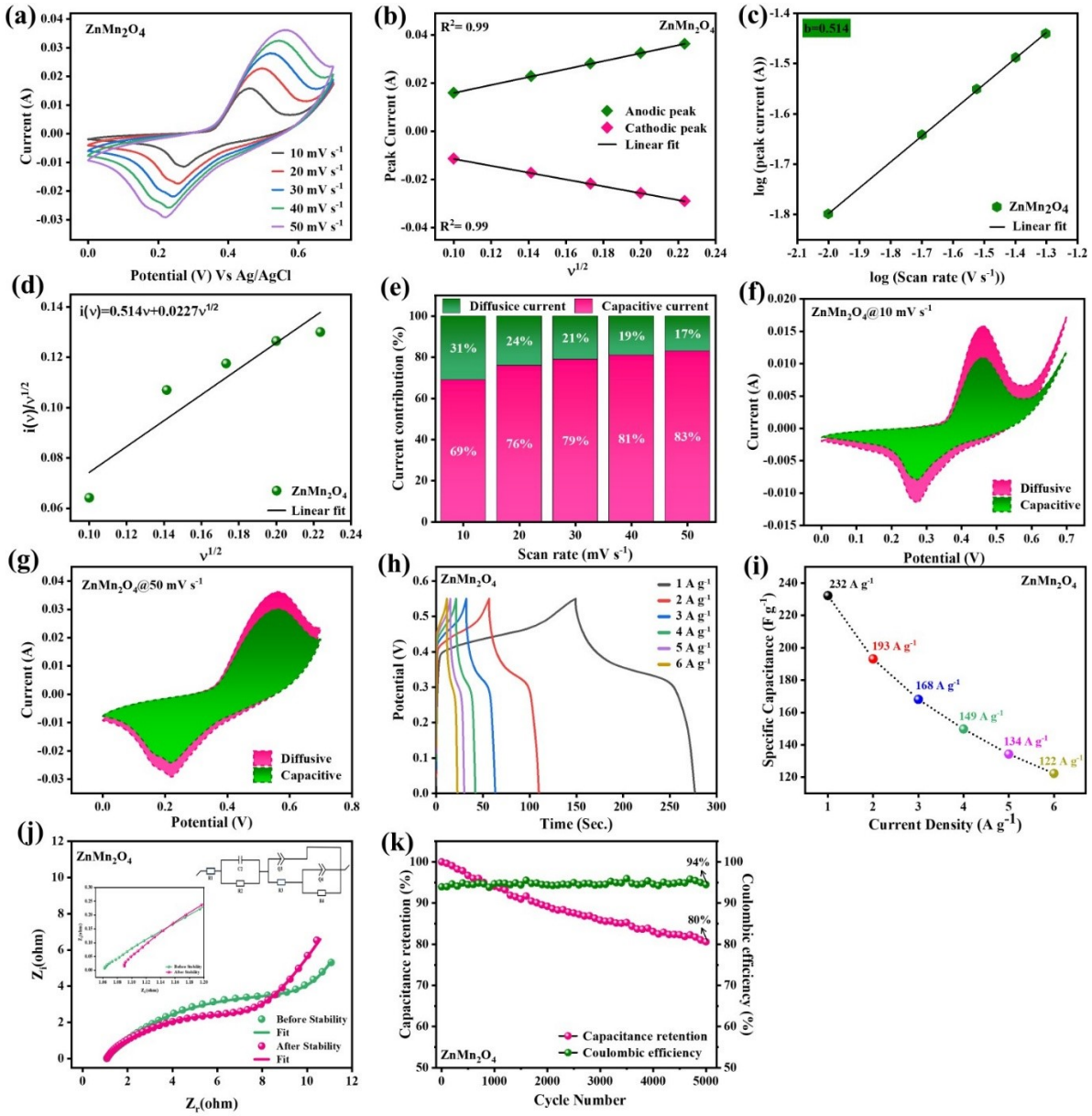

Figure S4. Electrochemical Analysis of $ZnMn_2O_4$ in a three-electrode system.

The electrochemical performance of Ni-MOF is also assessed utilizing a three-electrode configuration. The CV analysis of the Ni-MOF is performed at scan rates of 10 to 50 mV s^{-1}, with a potential of 0.8 V (vs Ag/AgCl) in 2 M KOH, as seen in **Figure S5a**. Increasing scan rates expose distinct redox peaks, validating the unique pseudocapacitive behavior attributed to rapid charge-transfer kinetics. The Randles-Sevcik equation determines the relationship between peak current (i_p) and the square root of scan rate ($v^{1/2}$) in anodic and cathodic responses. With an increase in scan rate from 10 to 50 mVs^{-1}, the anodic peak of the Ni-MOF shifts from 0.61 V to 0.72 V, reflecting a potential shift of 0.11 V, as depicted in **Figure S5b**. The observed elevation in anodic peak potentials for the Ni-MOF indicates a unique pseudocapacitive behavior influenced by electrochemical kinetics. The b-value of the Ni-MOF is determined to

be 0.356 (**Figure S5c**), showing battery and pseudocapacitive behavior characterized by predominant diffusion and surface-controlled faradaic reactions, since it is near 0.5. Dunn's technique is utilized to quantify the present contributions from surface-controlled and diffusion-controlled processes using **Equations S1 & S2** in the composite (**Figure S5d**). The bar graph illustrates that as the scan rate increases from 10 to 50 mV s^{-1}, the diffusion-controlled current decreases from 67 % to 48 % due to heightened internal diffusion resistance, whereas the capacitive current rises from 33 % to 52 %, as depicted in **Figure S5e**. The present contributions of Ni-MOF are clearly illustrated in the CV graphs depicted in **Figure S5f & g** at scan rates of 10 and 50 mV s^{-1}. The GCD measurement of the Ni-MOF was conducted at various current densities ranging from 1 to 6 A g^{-1}, as illustrated in **Figure S5h**, revealing a maximum specific capacitance of 450 A g^{-1} at 1 A g^{-1}, calculated using **Equation S3**. **Figure S5i** illustrates the specific capacitance of Ni-MOF at various current densities. Electrochemical impedance spectroscopy (EIS) is performed throughout a frequency range of 100 kHz to 100 mHz to analyze electron-transfer kinetics, interfacial interactions, and capacitive properties of the electrode material, as illustrated in the Nyquist plot in **Figure S5j**. The solution resistance (R_s) of the Ni-MOF is measured at 1.067 Ω before cycling and 1.26 Ω subsequent to cycling, while the charge transfer resistance (R_{ct}) is assessed at 1.829 Ω before cycling and 12.48 Ω following cycling. The capacitance retention (CR) and coulombic efficiency (CE) of the Ni-MOF electrode material were assessed across 5000 charge-discharge cycles at a current density of 10 A g^{-1}. The electrode demonstrated a lower capacitance retention (CR) of 58 % with a coulombic efficiency (CE) of 82 %, as determined by **Equation S4**, as depicted in **Figure S5k**.

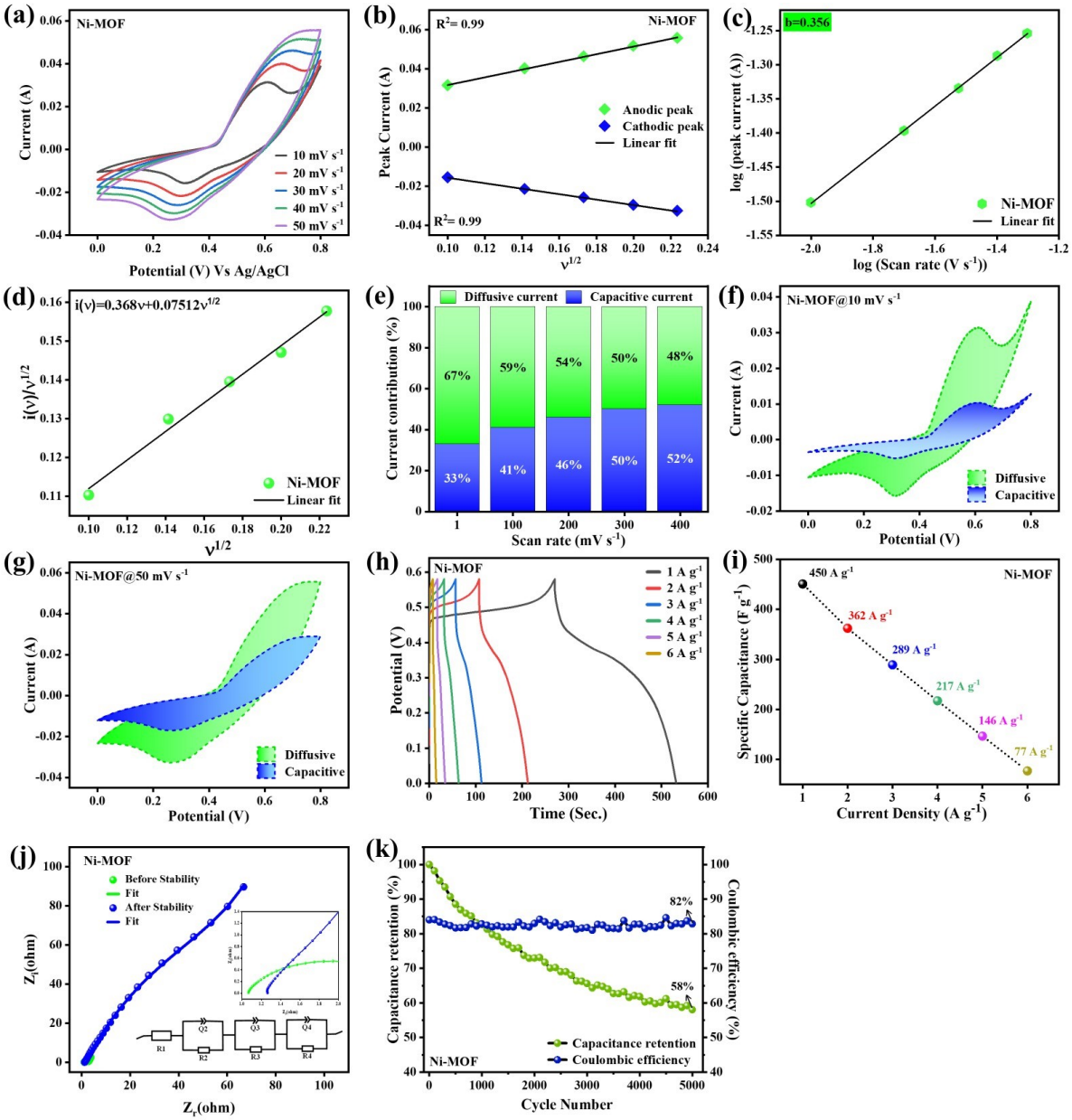

Figure S5. Electrochemical Analysis of Ni-MOF in a three-electrode system.

The $ZnMn_2O_4$/Ni-MOF composite exhibits enhanced electrochemical performance due to the synergistic combination of spinel $ZnMn_2O_4$ and Ni-MOF structures. The CV results validate distinct and reversible redox activity governed by Mn^{3+}/Mn^{2+} and Ni^{2+}/Ni^{3+} transitions in alkaline electrolyte. Kinetic analysis (b-value = 0.69 and Dunn's method) reveals a dominant diffusion-controlled pseudocapacitive mechanism with significant surface contribution, highlighting the hybrid charge-storage behavior. The composite delivers a higher specific capacitance of 623 F g^{-1} at 1 A g^{-1} with improved rate capability of 82% capacitance retention after 5000 cycles, along with 98% coulombic efficiency compared to the pure samples. EIS

analysis further indicates low solution resistance and acceptable charge-transfer resistance, confirming efficient ion transport and interfacial charge transfer in the composite. Overall, the enhanced electrochemical properties are attributed to the dual redox-active centres (Mn and Ni), improved electrolyte accessibility, shortened ion diffusion pathways, and strengthened interfacial coupling within the hybrid architecture, making the $ZnMn_2O_4$/Ni-MOF composite a promising electrode material for high-performance supercapacitor applications.

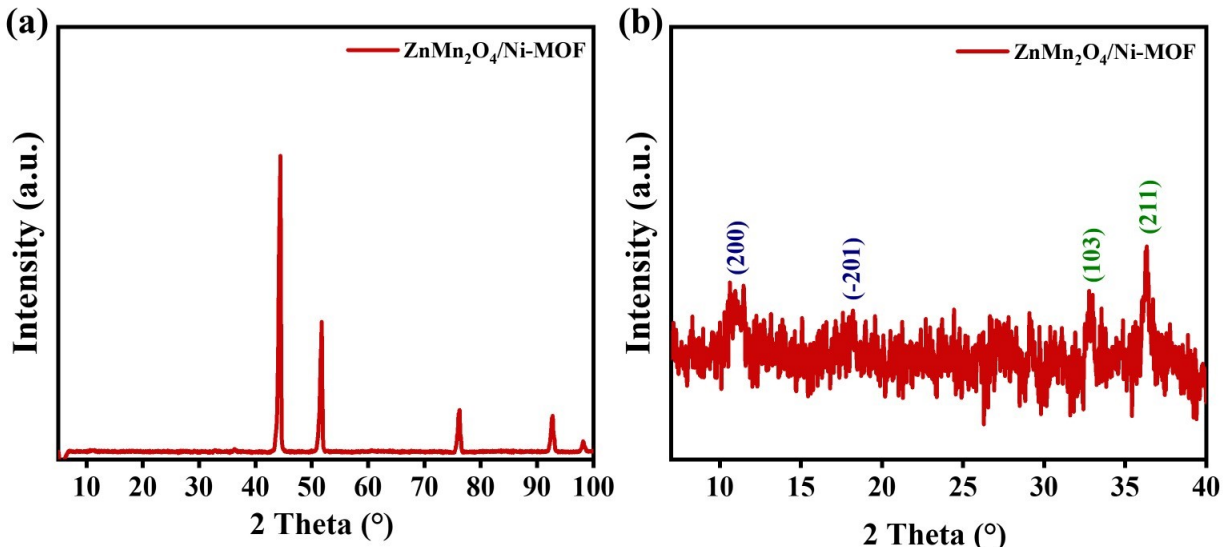

Figure S6. (a-b) Ex-situ X-ray diffractograms revealing the matching pattern of $ZnMn_2O_4$/Ni-MOF composite.

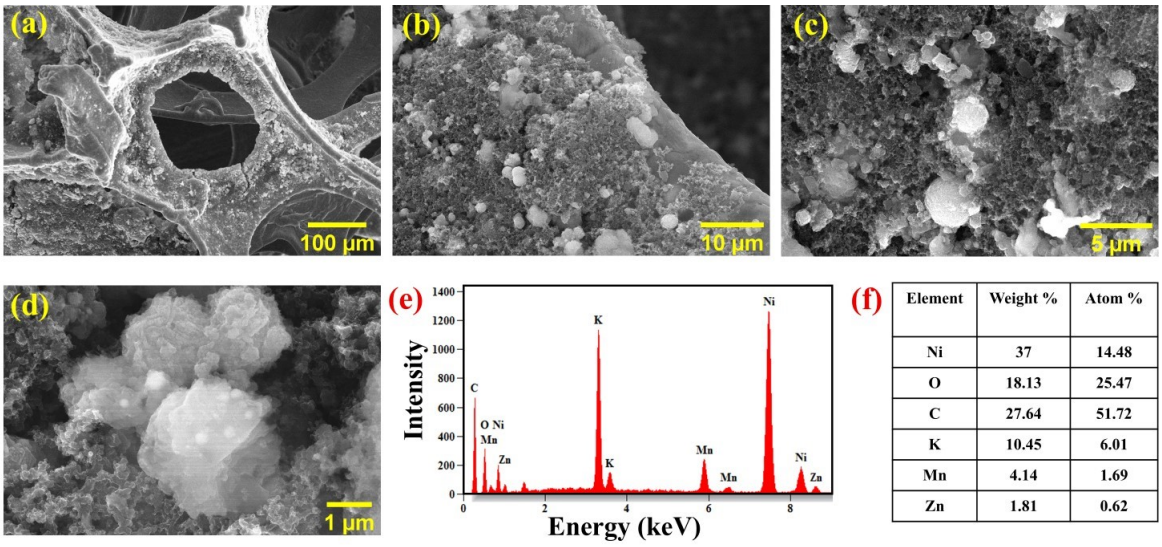

Element	Weight %	Atom %
Ni	37	14.48
O	18.13	25.47
C	27.64	51.72
K	10.45	6.01
Mn	4.14	1.69
Zn	1.81	0.62

Figure S7. (a-d) Ex-situ HR-SEM images of $ZnMn_2O_4$/Ni-MOF composite, and (e-f) EDX spectra revealing the stability of the active material in NF.

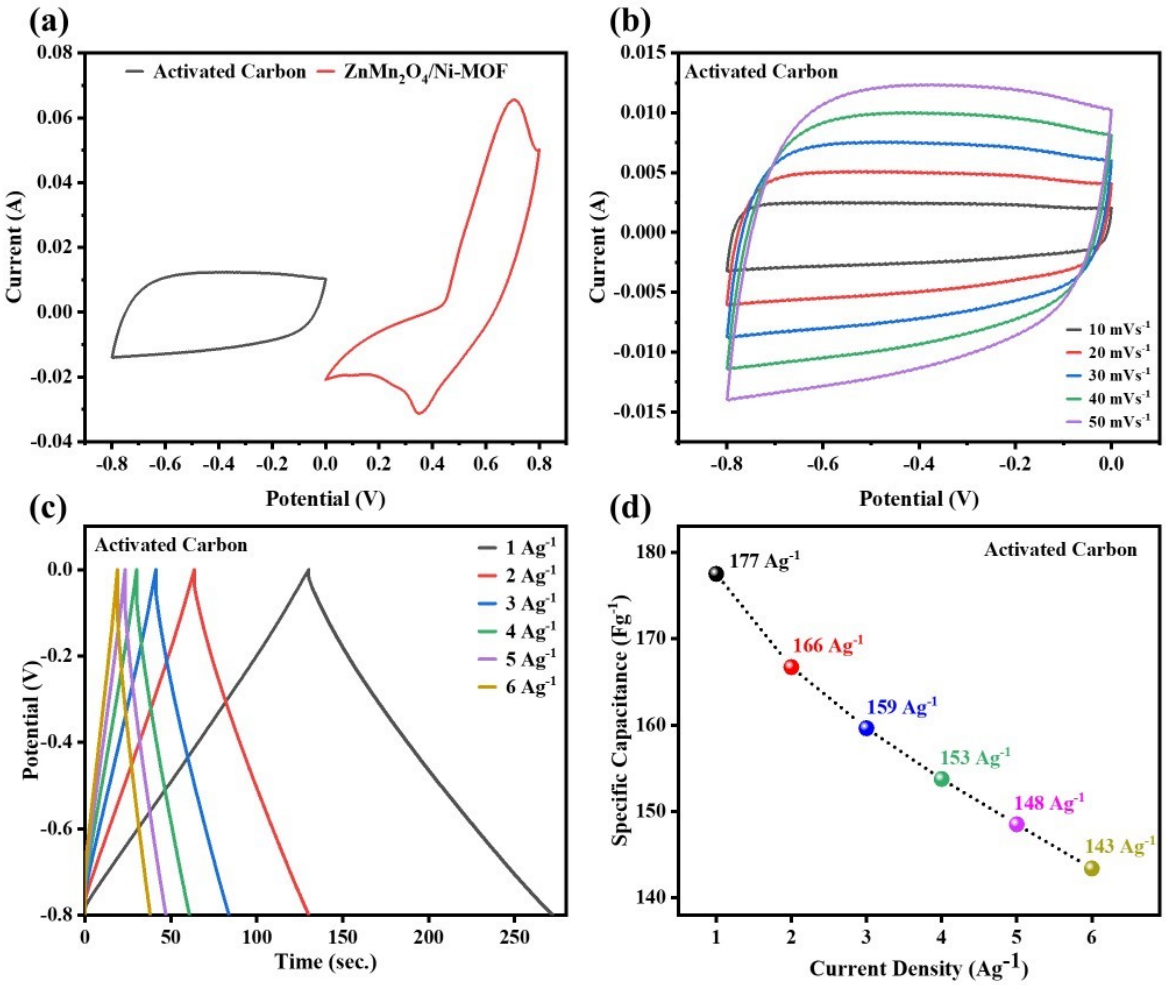

Figure S8. (a) The CV was recorded for the AC and $ZnMn_2O_4$/Ni-MOF composite in three electrode setups separately at 50 mVs^{-1} and then compared to find the ASC's operating voltage, (b) Three electrode studies of AC CV curves, (c) GCD curves, and (d) Specific capacitance for different current densities of AC.

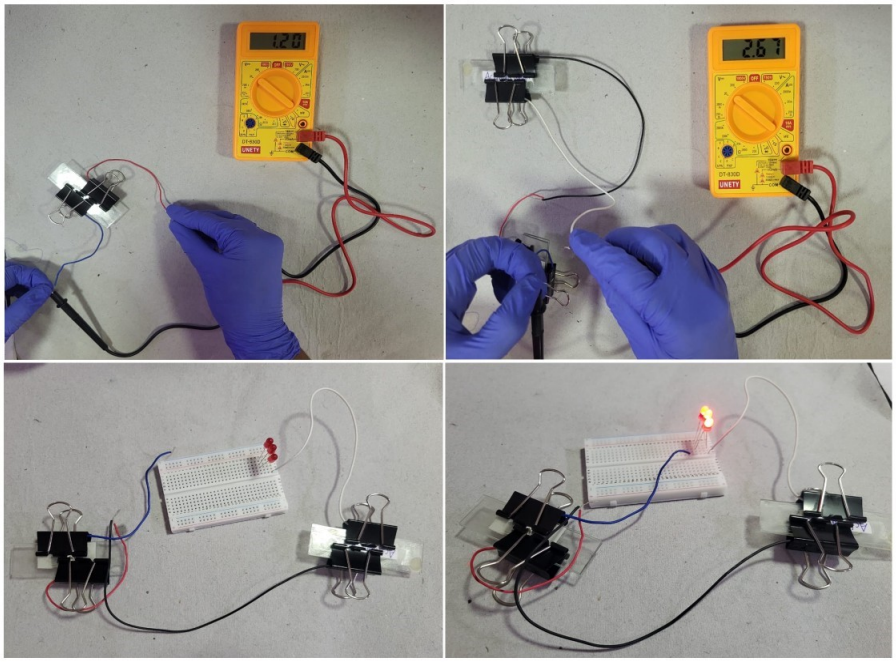

Figure S9. Asymmetric supercapacitor (ASC) devices successfully powered LEDs.

The electrochemical performance of the $ZnMn_2O_4$/Ni-MOF composite is particularly compared with that of pristine $ZnMn_2O_4$ and Ni-MOF under identical testing conditions. The cyclic Voltammograms (CV) of $ZnMn_2O_4$, Ni-MOF, and $ZnMn_2O_4$/Ni-MOF composite are compared at a scan rate of 50 mV s^{-1} is shown in **Fig. S10a**. The specific capacitance (C_s) of the $ZnMn_2O_4$, Ni-MOF, and $ZnMn_2O_4$/Ni-MOF composite determined from the CV using **Equation S8**:

$$C_s = \frac{\int I\,dV}{2mv\,\Delta V} \quad (Fg^{-1}) \qquad \textbf{S8}$$

where C_s - Specific capacitance, $\int I\,dV$ - Area of the CV curve, m - mass of the active material, ΔV - Potential window. The specific capacitance is found to be 154 F g^{-1}, 267 F g^{-1}, and 322 F g^{-1}, for $ZnMn_2O_4$, Ni-MOF, and $ZnMn_2O_4$/Ni-MOF composite at a scan rate of 10 mV s^{-1}. The significantly larger CV area of the $ZnMn_2O_4$/Ni-MOF composite electrode indicates superior charge-storage capacity, resulting from the synergistic interaction between $ZnMn_2O_4$ and Ni-MOF, which promotes higher redox activity and efficient ion-electron transfer. The specific capacitance comparison at different scan rates is shown in **Fig. S10b**. The GCD curves of $ZnMn_2O_4$, Ni-MOF, and $ZnMn_2O_4$/Ni-MOF composite are compared at a current density of 1 A g^{-1} (**Fig. S11b)**, and it shows a specific capacitance of 232 F g^{-1}, 450 F g^{-1}, and 623 F g^{-1}, calculated using the **Equation. S3**. The comparison of specific capacitance and current densities for the $ZnMn_2O_4$, Ni-MOF, and $ZnMn_2O_4$/Ni-MOF composite is shown in **Fig. S11c.**

The capacitance retention and coulombic efficiency of the $ZnMn_2O_4$, Ni-MOF, and $ZnMn_2O_4$/Ni-MOF composite are taken and compared as shown in **Fig. S11d&e**. In which the composite shows a retention and efficiency of 82.2 % and 98.3 %, compared to $ZnMn_2O_4$ (80.5 % retention and 94.4 % efficiency) and Ni-MOF (58 % retention, 82.8% efficiency). The $ZnMn_2O_4$/Ni-MOF electrode shows a superior specific capacitance compared to $ZnMn_2O_4$ and Ni-MOF, suggesting that the improved rate capability and cycle stability. The $ZnMn_2O_4$/Ni-MOF composite exhibits competitive or superior electrochemical performance, especially in specific capacitance, capacitance retention, and coulombic efficiency, due to the close nanoscale interaction between $ZnMn_2O_4$ and Ni-MOF. The findings indicate that the $ZnMn_2O_4$/Ni-MOF composite presents clear advantages compared to its individual components.

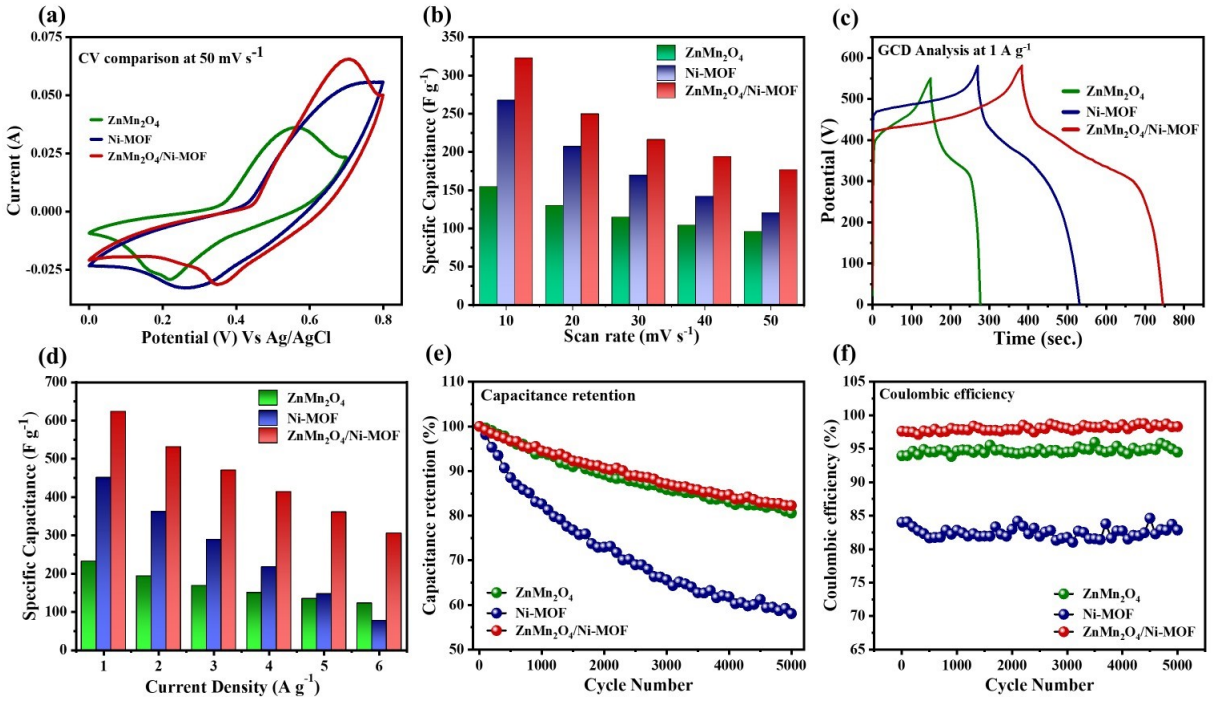

Figure S10. Comparative electrochemical analysis of $ZnMn_2O_4$, Ni-MOF, and $ZnMn_2O_4$/Ni-MOF composite a) Cyclic voltammetry (CV) at 50 mV s^{-1}, b) Specific capacitance calculated from the CV, c) Galvanostatic charge-discharge curves at 1 A g^{-1}, d) Specific capacitance calculated from the GCD, e) Capacitance retention, f) Coulombic efficiency.

BET Analysis of $ZnMn_2O_4$/Ni-MOF composite:

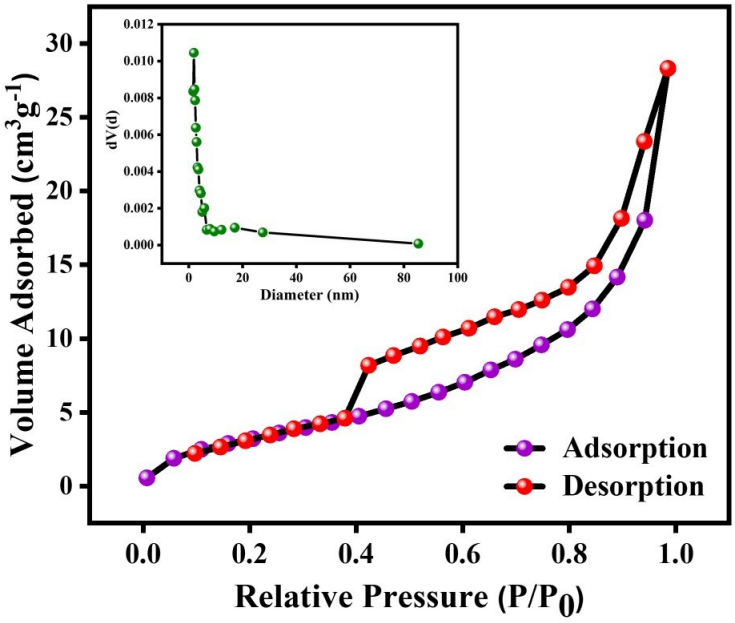

Figure S11. N_2 adsorption–desorption analysis of $ZnMn_2O_4$/Ni-MOF composite (inset: pore size distribution profile).

The surface area and porosity of the $ZnMn_2O_4$/Ni-MOF composite were obtained using N_2 adsorption/desorption isotherms. The isotherm exhibits a typical type IV isotherm (**Fig. S1**), indicating a predominantly mesoporous structure.[10] The pore size distribution reveals an average pore diameter of ~1.9 nm, located near the micro-mesopore boundary, suggesting the coexistence of small mesoporous with minor microporous contribution. The $ZnMn_2O_4$/Ni-MOF composite has a surface area of 13.25 m^2 g^{-1} and a pore volume of 0.051 cc g^{-1}, which enhances electrolyte infiltration and ion transport, accelerating ion diffusion within the electrode material and consequently improving electrochemical properties, as determined by the Brunauer-Emmett-Teller (BET) method.[11]

HR-TEM Analysis of the $ZnMn_2O_4$/Ni-MOF composite:

The structural evolution of the $ZnMn_2O_4$/Ni-MOF composite by HR-TEM at higher magnification clearly shows that the crystalline $ZnMn_2O_4$ nanospheres are intimately embedded within and surrounded by the Ni-MOF matrix, as shown in **Fig. S10 a-d**. The HRTEM images of the $ZnMn_2O_4$/Ni-MOF composite show well-resolved lattice fringes with interplanar spacings of 0.28 nm and 0.48 nm, corresponding to the (200) and (101) planes of crystalline $ZnMn_2O_4$, respectively, as shown in **Fig. S10e, f**.[4] The absence of lattice fringes in the Ni-MOF surface area is attributed to its intrinsic instability under intense electron beams[12]. The lattice fringes confirm the high crystallinity of $ZnMn_2O_4$ and are observed in direct contact with

adjacent lower-contrast Ni-MOF regions without any visible separation. The seamless interface in the $ZnMn_2O_4$/Ni-MOF composite demonstrates intimate nanoscale interfacial coupling between $ZnMn_2O_4$ and Ni-MOF.

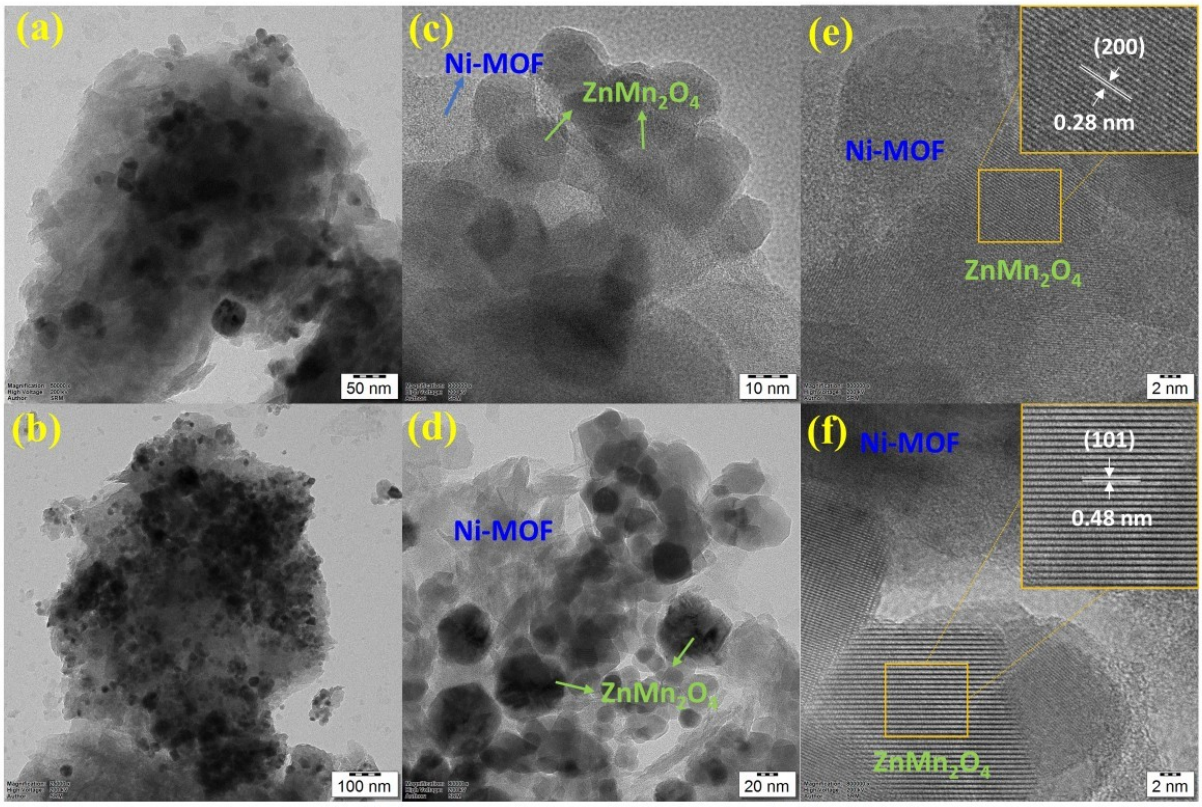

Figure S12. HR-TEM analysis of the $ZnMn_2O_4$/Ni-MOF composite.

Synergistic Effect:

To quantitatively compare the synergistic effect, the theoretical capacitance of the $ZnMn_2O_4$/Ni-MOF composite was calculated using the rule-of-mixtures model and compared with the experimentally obtained value.[13–15]

Experimentally calculated Specific capacitance at a current density of 1 Ag^{-1}:

$ZnMn_2O_4$ (C_1) - 232 F g^{-1}

Ni-MOF (C_2) - 450 F g^{-1}

$ZnMn_2O$/Ni-MOF (C_{exp} or C_3) - 623 F g^{-1}

Theoretical capacitance calculations:

Based on the weight percentage, we can take an approximately 1:1 ratio of $ZnMn_2O_4$ (w_1= 0.5 g) and Ni-MOF (w_2= ~0.5 g), then:

$C_t = w_1 C_1 + w_2 C_2$

$C_t = 0.5(232) + 0.5(450)$

$C_t = 116 + 225 = 341\ F\ g^{-1}$

The theoretical capacitance (C_t) of the $ZnMn_2O_4$/Ni-MOF composite is 341 F g^{-1}.

Synergistic Enhancement:

$$Synergistic\ Enhancement = \frac{C_{exp} - C_t}{C_t} * 100$$

$$= \frac{282}{341} * 100$$

$$Synergistic\ Enhancement = 82.7\ \%$$

$$Synergy\ factor = \frac{C_{exp}}{C_t}$$

$$= \frac{623}{341}$$

$$Synergy\ factor = 1.83$$

The experimental value significantly exceeds this theoretical value by a factor of 1.83, and this enhancement (83 %) quantitatively validates a synergistic interaction, presumably due to $ZnMn_2O_4$ particles inhibiting Ni-MOF aggregation and enhancing ionic conductivity at the heterostructure interface.

References:

1 P. Deva, S. Ravi and C. Manoharan, *Emergent Mater.*, 2024, **7**, 2407–2421.

2 H. Barkhordari, H. Heydari, A. Nosrati and J. Mohammadi, *Ionics (Kiel).*, 2019, **25**, 275–285.

3 D. Patel, S. N. Bariya, Y. G. Kapdi, P. Patel, A. Patel, V. Solanki, S. S. Soni and M. H. Patel, *J. Alloys Compd.*, 2025, **1014**, 178519.

4 V. Sannasi and K. Subbian, *Ceram. Int.*, 2021, **47**, 12300–12309.

5 P. K. Sharma, A. Sahai, D. Maikhuri, S. J. Uke, S. Asthana and Y. Kumar, *Journal of Materials Science: Materials in Electronics*, 2025, **36**, 1056.

6 A. S. Eliwa, S. S. Medany, G. G. Mohamed and M. A. Hefnawy, *J. Inorg. Organomet. Polym. Mater.*, DOI:10.1007/s10904-024-03559-6.

7 H. Wang, C. Zhu, M. Wu, F. Zheng, Y. Gao and H. Niu, *J. Mater. Sci.*, 2021, **56**, 2517–2527.

8 N. Manyani, P. Siwatch, S. Rana, K. Sharma and S. K. Tripathi, *Mater. Chem. Phys.*, 2025, **337**, 130562.

9 X. Li, J. Li, Y. Zhang and P. Zhao, *Colloids Surf. A Physicochem. Eng. Asp.*, 2021, **622**, 126653.

10 C. Zhang, D. Chen, Y. Luo, Y. Yuan, Y. Wang and Z. Yang, *Surfaces and Interfaces*, 2025, **56**, 105517.

11 T. Wu, J. Zhang, Y.-J. Gu, W. Wen, Z. Ye and J.-M. Wu, *J. Energy Storage*, 2025, **127**, 117189.

12 G. B. Bhanuse, S. Kumar, C.-W. Chien and Y.-P. Fu, *Electrochim. Acta*, 2025, **511**, 145371.

13 W. Shoukat, M. Z. Iqbal, I. Murtaza, P. Kanjariya, A. Rajiv, D. Shit, H. M. Albert, S. K. Samal, A. Kumar and S. M. Wabaidur, *RSC Adv.*, 2025, **15**, 25221–25232.

14 G. Pandey, S. Serawat and K. Awasthi, *ACS Nanoscience Au*, 2024, **4**, 399–408.

15 M. Kundu, S. Sau, S. Roy, S. Biswas, N. Bose, D. Mondal, B. K. Paul, R. Basu and S. Das, *J. Energy Storage*, 2026, **148**, 120204.